Journal of the European Ceramic Society 43 (2023) 1579–1589

Contents lists available at ScienceDirect

Journal of the European Ceramic Society

journal homepage: www.elsevier.com/locate/jeurceramsoc

Original Article

Residual stress effects of CMAS infiltration in high temperature jet engine ceramic coatings captured non-destructively with confocal Raman-based 3D rendering

Zachary Stein [a], Ravisankar Naraparaju [b], Uwe Schulz [b], Laurene Tetard [c], Seetha Raghavan [a,*]

[a] Department of Mechanical & Aerospace Engineering, University of Central Florida, Orlando, FL, 32816, USA
[b] Institute of Materials Research, German Aerospace Center (DLR), Cologne, 51170, Germany
[c] Department of Physics, NanoScience Technology Center, University of Central Florida, Orlando, FL, 32816, USA

ARTICLE INFO

Keywords:
CMAS
TBCs
Raman spectroscopy
Residual stress
EB-PVD

ABSTRACT

Calcium-magnesium-aluminosilicates (CMAS) are ingested by jet engines and infiltrate into high temperature ceramic coatings during operation. This infiltration increases coating stiffness and promotes coating phase destabilization, encouraging micro-crack formation. Thermomechanical effects from CMAS infiltration were mapped over time with confocal Raman spectroscopy through residual stresses within EB-PVD 7YSZ coatings with microscale resolution. The results show an interplay between physical and chemical components influencing the residual stress. Physical mechanisms influence residual stress more after 1h of infiltration, inducing tensile loading up to 100 MPa on tetragonal ZrO_2 Raman bands. Chemical mechanisms impart greater influence after 10h, inducing compressive loading up to 100 MPa. A monoclinic phase volume fraction of about 35% was observed as a transitional point for chemical mechanisms overtaking physical mechanisms in influencing residual stress. These results non-destructively elucidate changes within a coating's residual stress during CMAS infiltration, aiding coating degradation monitoring during maintenance and towards implementing CMAS-mitigation strategies.

1. Introduction

Metallic alloy components operating within extreme conditions, such as turbine blades within gas turbine jet engines, are commonly protected by high temperature ceramic layers referred to as thermal barrier coatings (TBCs). These high temperature coatings provide a temperature gradient of approximately 200 °C with respect to the hot environment [1]. TBCs are typically coupled with additional cooling methods, such as film cooling, to increase the temperature gradient from the hot gases produced by the combustion section of the engine in order to further improve the performance, durability, and to extend the life of the hot section components [2–5]. Standard TBCs comprise of several layers including a ceramic top coating, a thermally grown oxide layer (TGO) that forms throughout the life cycle of the coating, and a metallic bond coat to aid in adhesion between the ceramic coating and the metallic superalloy [6]. An industry standard material used for the ceramic top coats is 7 wt% yttria partially stabilized zirconia (7YSZ), corresponding to approximately 4 mol% Y_2O_3-ZrO_2, due to its low thermal conductivity and mechanical strength [2,7]. Several methods have been considered for depositing TBCs, such as air plasma spray (APS) and electron-beam physical vapor deposition (EB-PVD). EB-PVD, the deposition method used within this study, produces characteristic closed-porosity columnar structures, which provide high in-plane strain tolerance, lower thermal conductivity, and excellent thermal shock protection. These attributes are ideal for moving components, such as turbine blades [8,9]. However, 7YSZ coatings are still susceptible to severe mechanical and chemical degradation that can threaten the safety of hot section components and the engine itself, when operating in harsh environments. Exposure to contaminants from the external environment of the engine can have detrimental effects on the effectiveness and operational lifetime of TBCs [10–14].

During operation, jet engines are subjected to a variety of environmental conditions that can translate into airborne contaminants entering the engine. Such contaminants are calcium, magnesium and alumino-silicates (CMAS) dominated sand or volcanic ash. CMAS is ingested into the engine and becomes molten due to the high temperatures of the combustor during operation. This molten CMAS melt is then carried to the turbine section of the engine and is then deposited onto the turbine blades. The molten CMAS rapidly infiltrates into the

* Corresponding author.
E-mail address: seetha.raghavan@ucf.edu (S. Raghavan).

https://doi.org/10.1016/j.jeurceramsoc.2022.11.003
Received 17 April 2022; Received in revised form 7 October 2022; Accepted 1 November 2022
Available online 5 November 2022

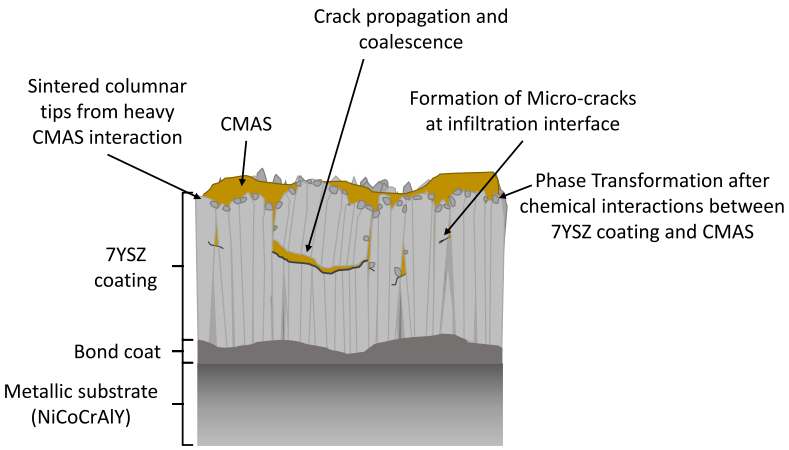

Fig. 1. Schematic of a standard TBC composition. A TBC comprises of a metallic substrate, bond coat, and 7YSZ top coat, infiltrated by CMAS and some effects from this infiltration. These effects include the sintering of columnar tips and of the feather arms, micro-crack formation, propagation, and coalescence until causing localized coating delamination, and the localized formation of freely transformable ZrO_2 from the 7YSZ top coat.

coatings and fills the intercolumnar gaps of the top coat for EB-PVD coatings, such as 7YSZ, through strong capillary effects [9,10,12,15,16].

The depth at which CMAS infiltrates into the coating as well as the extent and rate of coating degradation is dependent on a variety of factors regarding the CMAS composition, its viscosity, the microstructure and material properties of the coating, the thermal gradient present throughout the coating, the ambient hot gas temperature, and environmental conditions such as humidity within the turbine section [9,17]. Similarly, the existing literature has found a critical depth of infiltration, beyond which the coating is highly susceptible to delamination failure [18]. CMAS begins to solidify within the coating as it infiltrates through the coating and reaches cooler temperatures below its melting point due to the temperature gradient present within the coating. The solidified CMAS effectively combines the columns together and stiffens the overall coating. This columnar stiffening decreases the strain tolerance, introduces mismatching coefficients of thermal expansion, and increases the overall thermal conductivity of the coating [13,19–21]. The now sealed intercolumnar gaps are unable to provide relief to the columns during cycling. If the CMAS has not fully infiltrated throughout the coating and its intercolumnar gaps before cooling, two distinct regions form through the depth of the coating [22]. The infiltrated region will experience additional tensile stresses with the increased stiffness and decreased coating porosity [10,20,21,23]. This bulk region also induces bending forces onto the interface between the infiltrated and non-infiltrated regions. The resulting residual stresses present within the coating coupled with thermal loading and coefficient of thermal expansion mismatches between these two regions of the coating during operating, if severe enough stresses are present, will cause microcracks to form and coalesce, leading to localized delamination and eventual premature coating failure at this infiltrated and non-infiltrated interface [12,21,24].

Additional chemically-induced stresses form within the coating as it interacts with the molten CMAS and becomes destabilized. Primarily, yttria, used to stabilize ZrO_2 into the tetragonal state, referred to as tetragonal-prime, is leeched from the coating into the CMAS melt over time. Small amounts of the ZrO_2 are also leeched into the CMAS. However, the ZrO_2 quickly becomes saturated within the melt as compared to the yttria [25–28]. This interaction between the CMAS melt and YSZ coating contributes to the sintering of columnar tips and feather arms on the edges of the columns. Without yttria to stabilize the ZrO_2 polymorph, the yttria-lean coating can freely transform from its once stable tetragonal-prime phase to an yttria-lean tetragonal, cubic, or monoclinic phases [12,21,25,26,29]. The monoclinic phase itself poses several problems with its associated volumetric increase in the lattice structure of about 3%–5% [30,31]. The monoclinic phase has been found to start forming around 600 °C and lower [32]. This expansion introduces additional residual stresses, which contribute towards the premature failure of the coating [9,10,13,18,20,21,24,30,31,33,34]. This thermochemical mechanism of phase destabilization and transformation is delayed and much slower acting than the thermomechanical effects of CMAS infiltration through CMAS-induced coating stiffening [26,35].A schematic demonstrating the effects of CMAS infiltration into 7YSZ TBCs on the residual stress is displayed in Fig. 1. In this work, further elucidation will occur for the residual stress evolution effects of CMAS infiltration into 7YSZ EB-PVD TBCs over time through a non-destructive confocal Raman spectroscopy technique [36,37].

Raman spectroscopy can be used to distinguish the distinct chemical phases of ZrO_2 polymorphs [38]. For instance, previous work by the authors have demonstrated the non-destructive evaluation in the formation of the monoclinic phase over increased annealing times with a high spatial resolution using confocal Raman spectroscopy and 3D rendering [36,37,39]. Additionally, Raman spectral signatures can be used to quantify stress through changes in the vibrational frequency of these chemical bonds as a result from by both residual and additional externally applied stresses [21,40,41]. Though spatial resolution of Raman mapping is limited by diffraction, the coupling of the spectral measurements with confocal microscopy has significantly improved the lateral and depth precision that can be attained with the technique. In the case of 7YSZ, both the phase of ZrO_2 and the stress states in the coat can be determined non-invasively, including below a sample's surface, to form three-dimensional (3D) reconstructions of the material properties. It is within this probed volume that the extent of CMAS-induced coating degradation can be evaluated on a localized microstructure level.

Within this study, the residual stress evolution is tracked for 7YSZ EB-PVD coatings infiltrated by CMAS at an annealing temperature of 1250 °C as a function of varying annealing times of 1 h and 10 h and depth through 3D reconstructing confocal Raman spectroscopy measurements. The annealing temperature of 1250 °C was selected since this temperature is higher than the melting point of this particular CMAS composition and, as a result, the CMAS remains in a melt state throughout the entire annealing time. Further investigations regarding the CMAS composition used within this study and its melting point may be found in [13]. An additional sample that was not infiltrated was also annealed at 1250 °C for 10 h to serve as a stress reference for the residual stress state of the coating without CMAS attack in order to isolate the effects of CMAS infiltration on a coating's residual stress within a given probed volume. The stress was evaluated through the Raman shifts in the 643.78 cm^{-1} tetragonal

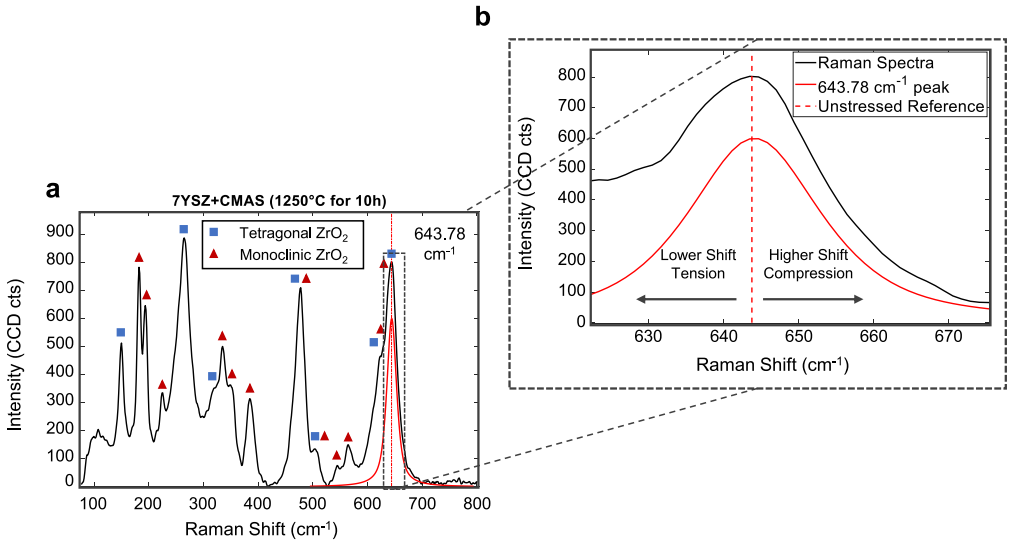

Fig. 2. Raman spectra of CMAS-infiltrated 7YSZ. (a) Raman spectra of CMAS infiltrated 7YSZ coating after an annealing time of 10 h at an annealing temperature of 1250 °C. The associated Raman peaks for the tetragonal and monoclinic ZrO_2 phases are labeled with squares and triangles, respectively. (b) Expanded view of the tetragonal 643.78 cm^{-1} peak used within this study. Induced stresses are evaluated by the shifts with respect to this 643.78 cm^{-1} peak corresponding to the unstressed material.

ZrO_2 Raman band from a stress reference state determined by Tanaka et al. [42]. The residual stress of the coating was also evaluated using the 463.7 cm^{-1} tetragonal ZrO_2 Raman band for validation using a stress reference state mentioned by Krämer et al. [21]. An additional comparison of the Raman shifts between the tetragonal and monoclinic ZrO_2 Raman bands were performed using a stress reference state determined by Barberis et al. [43]. Stress was then quantified for both the 643.78 and 463.7 cm^{-1} tetragonal Raman bands using a Raman shift and piezo-spectroscopy relationship stress equation with piezo-spectroscopic coefficients found by Tanaka et al. and Bouvier & Lucazeau, respectively [42,44]. Using the 3D reconstruction method described in a previous investigation [39], a 3D map of the residual stress evolution within the 7YSZ EB-PVD TBC system was reconstructed showing the effects of annealing time throughout the probed depth with a microscale resolution. Additionally, comparison and correlation calculations were performed to elucidate the relationship between the monoclinic formation and its phase volume fraction concentration relative to the residual stress state of the coating.

2. Material and methods

2.1. 7YSZ TBC fabrication

A 150 kW electron-beam physical vapor deposition (EB-PVD) system at the German Aerospace Center (DLR) in Cologne, Germany was used to produce 400 μm 7YSZ coatings deposited onto alumina substrates. These coatings were intentionally produced with higher thicknesses to isolate and to study the CMAS infiltration kinetic effects in EB-PVD coatings. Potential effects from the substrate are minimized by taking a control sample annealed without any CMAS infiltration. This not only provides a baseline, but also isolates the residual stresses induced only by CMAS infiltration. During the deposition process, the alumina substrates used were placed on a sample holder with a rotational speed of 12 rpm directly above the YSZ ingot with a substrate temperature of 1000 °C. More information regarding the sample fabrication and manufacturing can be found in [39].

2.2. CMAS composition and fabrication

The CMAS composition was derived from compositions found within aero-engines operating within Middle Eastern countries (in mol.%: 24.6% CaO, 12.4% MgO, 11% Al_2O_3, 41.7% SiO_2, 8.7% FeO & 1.6% TiO_2) as previously described in [9,39]. The CMAS powders were artificially synthesized through the co-decomposition of SiO_2 and TiO_2 as well as Me-nitrates powders. The process of this producing these CMAS powders are described in greater details in [9].

Table 1
Samples information regarding composition, annealing temperature, and annealing time.

Sample	Composition	Temperature (°C)	Time (h)
A3	7YSZ	1250	10
B2	7YSZ + CMAS	1250	1
B3	7YSZ + CMAS	1250	10

2.3. CMAS infiltrated TBC preparation

A paste of CMAS in a concentration of 10 mg/cm^2 was applied on the 7YSZ coating and infiltration experiments were performed at an annealing temperature of 1250 °C and with heating and cooling rates of 10 K/min in a laboratory box furnace. Two annealing times of 1 h and 10 h were selected to understand short-term and long-term infiltration kinetic effects of molten CMAS in 7YSZ coatings and to provide initial observations on the time dependency effects of CMAS infiltration with respect to coating stress evolution. The authors plan to expand upon this work on full coating systems with higher temporal resolutions focusing in critical time regimes based on the findings from this study. A summary of the samples within this study is provided in Table 1. A control sample composed purely of 7YSZ without any CMAS infiltration (A3) was used as a reference to rule out the effect of high temperature annealing on 7YSZ and to serve as a reference to focus solely on the resulting effects of CMAS infiltrated in 7YSZ for the chosen 1 h (B2) and 10 h (B3) annealing times. Validation was performed on a cross section of a CMAS infiltrated TBC annealed for 10 h (B3). More information on the validation measurements carried out on this cross-sectioned sample to the probed volume with the confocal non-destructive approach used within this study can be found in [39].

2.4. Raman measurements parameters

An Alpha 300RA WITec Confocal Raman microscope equipped with a He:Ne 532 nm laser source excitation was used to perform Raman measurements. A 20× objective lens with a numerical aperture of 0.4 (corresponding to a Z-resolution of 6.65 μm and XY-resolution of 0.8 μm)

was used. An excitation laser power of 11 mW and additional collection parameters, including an integration time of 20 s, remained constant for all the data reported in this study. The Rayleigh scattering was filtered with a notch filter and the inelastically scattered light was split with an 1800 g/mm grating. A step size of 1 μm was used for the line scans and 2D maps as to prevent potential overlapping of probed points from the theoretical 0.8 μm lateral resolution. Each 2D map consists of an array of 20 × 20 spectra, corresponding to 400 spectra being collected for a total acquisition time of 8000 s. The detection spectral range covered during these measurements range between 100–800 cm^{-1}. 2D Raman spectral maps at increasing depths were collected by focusing the light at increasing positions beneath the surface to assess CMAS degradation by the corresponding localized residual stress changes in 7YSZ. The step size between these different depth planes was 6.65 μm, which corresponds to the axial resolution limit for the 20× objective lens used within this study.

3. Calculations

The Raman shift and its association with stress can be written as Eq. (1):

$$\Delta\sigma \approx \frac{\upsilon - \upsilon_0}{\Pi} \tag{1}$$

where $\Delta\sigma$ is the change in stress, υ is the measured peak position, υ_0 is the referenced peak position, and Π is the linear piezo-spectroscopic coefficient that is experimentally found. Work by Tanaka et al. has found that the piezo-spectroscopic coefficient for the tetragonal 643.78 cm^{-1} peak in a freestanding 7YSZ EB-PVD is 5.43 cm^{-1} GPa^{-1}. It is from Eq. (1) that the residual stress the coating experiences from CMAS attack can be quantified from the tetragonal phase of the coating. The stresses of other peaks may also be quantified using Eq. (1) so long as the piezo-spectroscopic coefficient has been determined for the stress-resolved peak.

3.1. Analysis of Raman spectra

The monoclinic and tetragonal ZrO_2 phases have doublets located between 600–650 cm^{-1} Raman shift [44–47]. More specifically, the peak position references used within this study for the monoclinic doublets are located at 615.2 cm^{-1} [43] and 637.6 cm^{-1} [43]. Meanwhile, the peak position references used for the tetragonal doublets are located at 607.1 cm^{-1} [43] and 643.78 cm^{-1} [42]. These peak positions are indicated as vertical dashed lines in Fig. 3. These high convoluted peaks present an issue when fitting the tetragonal 643.78 cm^{-1} peak. Therefore all four peaks must be deconvoluted in order to isolate the 643.78 cm^{-1} peak prior to quantifying the residual stress of the coating using Eq. (1). These four peaks were deconvoluted using a nonlinear least squares solver within MATLAB and were fitted using a pseudo-Voigt function. The mPVF values found in a previous investigation reported in [39] and relative peak relationships including the intensity ratios and full width at half maximum peak values were used as additional initial parameter values for defining the pseudo-Voigt function. An example of the final results of this deconvolution for both the monoclinic and tetragonal doublets as well as the residual, signal-to-noise ratio, and normalized root mean square equation (NRMSE) goodness of fit equation where 1.0 is a perfect fit is shown in Fig. 3.

The stress reference peak position reference and the piezo-spectroscopic coefficient reported by Tanaka et al. is used for the 643.78 cm^{-1} tetragonal ZrO_2 Raman band since their measurements were conducted on a free standing 7YSZ EB-PVD coating [42]. This allows for the changes in the residual stress solely due to the coating's interaction with CMAS to be more accurately quantified when coupled with the PS-coefficient. This stress reference peak position takes into account the stresses induced to the ZrO_2 bonds when structured through EB-PVD spray as compared to ZrO_2 nano-powder.

A 2D stress map for each depth was obtained by applying Eq. (1) to each deconvoluted 643.78 cm^{-1} peak in every point of the 2D map. These 2D maps were then stacked by their respective probed depths creating a 3D reconstruction of the probed volume. This reconstruction was performed for each sample by compiling and importing the sequence of 2D maps into the volume viewer plugin with a trilinear interpolation within ImageJ.

4. Results

A Raman spectrum of CMAS infiltrated 7YSZ coating is shown in Fig. 2(a). This specific lineout comes from a sample that was exposed to CMAS and annealed isothermally for 10 h at 1250 °C, allowing for substantial phase transformation to occur during the annealing process. With the finest grating available on this instrument, Raman spectroscopy is unable to directly distinguish between the peaks within the yttria-rich stabilized tetragonal-prime phase and the similar yttria-lean transformable tetragonal phase, so the peaks associated with both have been labeled as the tetragonal phase throughout this paper. Similarly, the cubic phase has very broad peaks in the same range as the tetragonal phase located around 620 cm^{-1}. It was found that the inclusion of these broad cubic peaks during data analysis made negligible differences in the results and are therefore not reported in the results of this study. The tetragonal and monoclinic phases and their peak positions have been labeled in Fig. 2(a). Previous literature has found the tetragonal peak labeled at 643.78 cm^{-1} is also stress sensitive and an excellent candidate for quantifying the stress within tetragonal ZrO_2. An expanded view of the 643.78 cm^{-1} peak is shown in Fig. 2(b). The unstressed reference of the tetragonal 643.78 cm^{-1} peak used within this study is based on a full freestanding EB-PVD 4 mol% YSZ coating from Tanaka et al. [42]. From this unstressed reference peak position, any shifts could be attributed to additional stresses introduced to the coating as a result of CMAS infiltration. A shift to a lower relative wavenumber corresponds to a chemical bond associated peak in the coating experiencing tension, also known as a redshift. Likewise, if the measured peak shifts to a higher relative wavenumber, then the coating is experiencing compression, also known as a blueshift. An experimentally determined piezo-spectroscopic coefficient associated with the 643.78 cm^{-1} peak can then be used to quantify the stress the coating is experiencing [44]. Similar to tracking degradation through the phase concentration [39,43], using this Raman shift and piezo-spectroscopic coefficient stress relationship equation, Eq. (1) allows for tracking the stress evolution throughout CMAS-induced degradation of the coating. It is from quantifying the stress in multiple 2D Raman hyperspectral maps at increasing depths in the coating that a 3D reconstruction can be created to track the residual stress evolution of the coating as a result of CMAS degradation throughout a probed volume.

Using the stress calculation method detailed above, volumetric reconstructions of the Raman stress are considered for non-infiltrated sample A3, annealed at 1250 °C for 10 h (Fig. 4(a)), and for CMAS infiltrated samples B2 and B3, annealed at 1250 °C for 1 h and 10 h Fig. 4(b,c), as well as the average stresses throughout the depth of the probed volume Fig. (4(d)). The non-infiltrated A3 sample serves as a stress reference of the 7YSZ EB-PVD coating prior to infiltrated and can therefore be compared to the CMAS infiltrated samples. The non-infiltrated sample also serves as a reference to evaluate the effects CMAS infiltration has on the residual stress for sample B3, both of which have been annealed at the same temperature and duration.

It can be observed that the non-infiltrated sample has a very uniform stress state after being annealed for 10 h at 1250 °C (Fig. 4(a)). Compression estimated at 100 MPa was calculated throughout the volume of the coat. This compression within the probed volume of the coating is typical for columnar microstructures of EB-PVD coatings [48]. As a non-infiltrated EB-PVD coating ages, the gradient of compressive stress coming from the growth of the thermally grown oxide layer at the interface is expected to increase as the thermal grown oxide layer

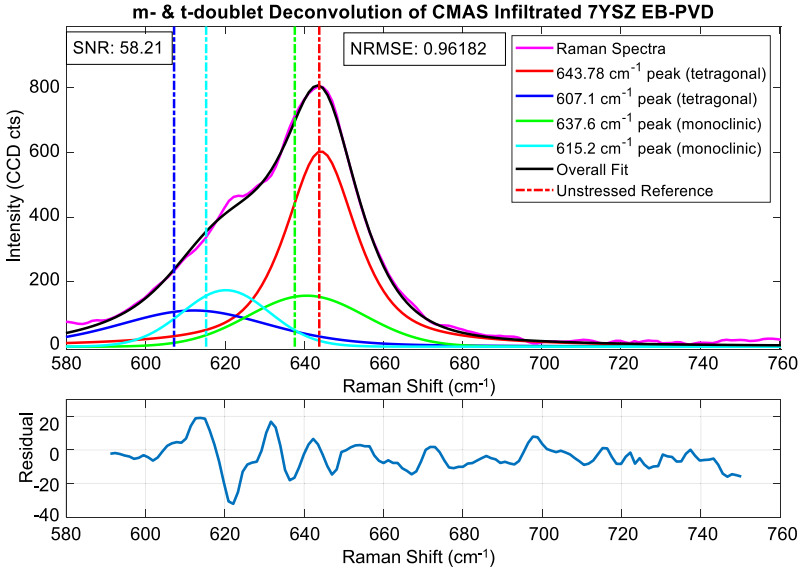

Fig. 3. Deconvolution of the monoclinic and tetragonal doublets around the 643.78 cm^{-1} peak. The measured Raman spectrum is shown in pink while the summation of the pseudo-Voigt function fitted peaks is in black. The unstressed reference peak positions of 607.1, 615.2, 637.6, and 643.78 cm^{-1} are marked in dashed lines corresponding to their respective fitted peak's colors of blue, cyan, green, and red, respectively. The unstressed reference peak positions are based on the findings in [42,43]. The 607.1 and 643.78 cm^{-1} peaks correspond to the tetragonal phase doublet while the remaining 615.2 and 637.6 cm^{-1} peaks correspond to the monoclinic phase doublet. Additional measurement and goodness of fit parameters are also shown through the signal-to-noise ratio and the normalized root mean square equation goodness of fit, shown as SNR and NRMSE, respectively, in the figure. For the goodness of fit, 1.0 is an ideally perfect fit. The residual differences between the fitted and measured peaks are plotted in the lower graph. (For interpretation of the references to color in this figure legend, the reader is referred to the web version of this article.)

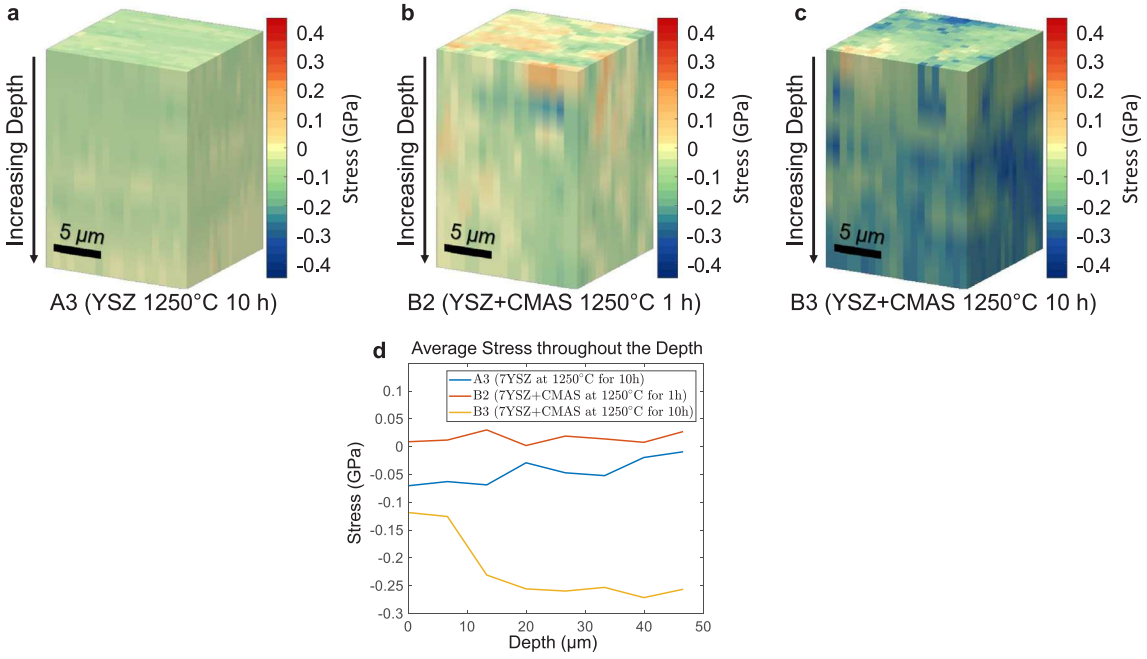

Fig. 4. 3D reconstruction of the residual stress from the 643.78 cm^{-1} peak. (a) a non-infiltrated 7YSZ sample annealed at 1250 °C for 10 h (A3), (b) a CMAS infiltrated 7YSZ sample annealed at 1250 °C for 1 h (B2), and (c) a CMAS infiltrated 7YSZ sample annealed at 1250 °C for 10 h. (d) Average stress as a function of depth for A3, B2 and B3. (For interpretation of the references to color in this figure legend, the reader is referred to the web version of this article.)

becomes more developed early in a coating system's lifetime, causing the coating to experience more compression [48].

CMAS exposure and infiltration is observed to have an effect on the stress state of the coating in Fig. 4(b–d). After 1 h of infiltration, the overall average stress state of the coating becomes slightly tensile, as observed in the red line in Fig. 4(d). The tensile loading is likely a result of both the coating stiffening from CMAS infiltrating the intercolumnar gaps of the coating as well as coating sintering [24]. Additionally, non-uniform stresses appear in the probed volume of the coating in Fig. 4(b). While some regions still display a similar stress state to that of the non-infiltrated sample, other regions are experiencing around 100 MPa of tension. This variation can be attributed to the local microstructure of the coating. While molten, CMAS infiltrates throughout the intercolumnar gaps and feather arms of the EB-PVD columns and then solidifies before stiffening the coating upon cooling [9,16,49]. As a result, there are higher concentrations of CMAS within these

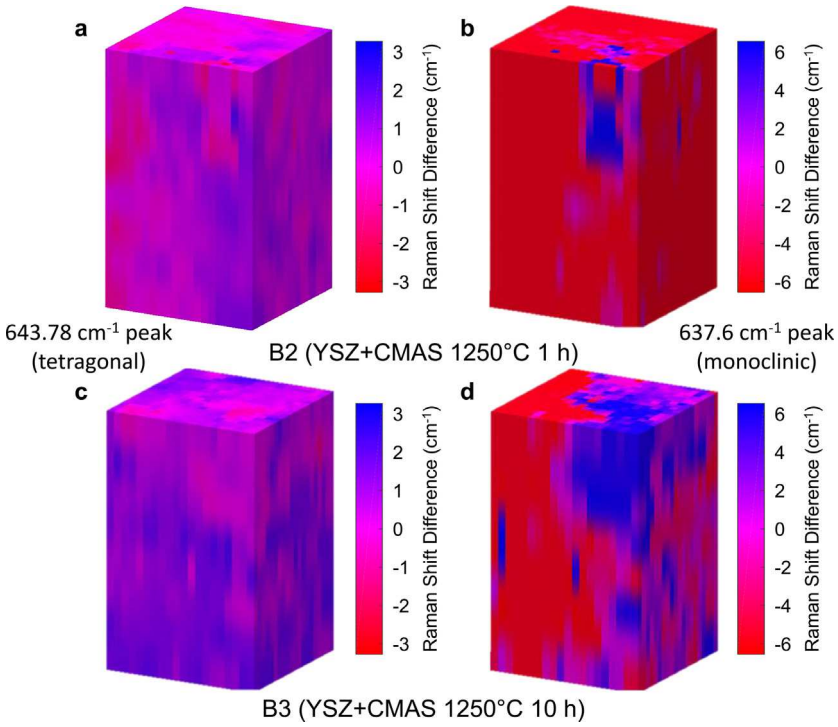

Fig. 5. 3D reconstruction based on Raman shifts. Raman shifts for CMAS infiltrated 7YSZ samples annealed at 1250 °C at (a) 1 h and (b) 10 h. Shifts are relative to the unstressed peak position references in [42,43].

intercolumnar gaps. This is not only observed with higher monoclinic concentrations as in [39], but also within the residual stresses of the coating. While other factors will influence the overall residual stress state within the microstructure, there will be a trend towards a red shift, tension, for the edges of the 7YSZ columns as well as any coating surfaces in contact with CMAS.

After 10 h of infiltration, as seen in Fig. 4(c), the overall stress state of the coating drastically changes, shifting to an average state of compression. While there still are small regions of tension, as observed after 1 h of infiltration, a majority of the coating is ranging from around 100 MPa of compression at the surface to around 300 MPa of compression around 46 μm into the depth of the coating, noted in the yellow line in Fig. 4(d). As compared to the non-infiltrated sample, which was also annealed for 10 h at 1250 °C, the average stress state of the coating overall is also more compressive on and around the edges of the columns. This higher stress state of compression as well as the minor shift from tension to compression in most regions can be attributed to phase destabilization and subsequent phase transformation of the coating. Additionally, this trend towards of a residual stress profile first becoming more tensile and then transforming to become more compressive with increased CMAS exposure and annealing times aligns with what has been found in literature [21,50,51].

Volumetric reconstructions of the Raman stress-induced peak shifts are shown in Fig. 5 for both the 643.78 cm^{-1} tetragonal peak of B2 and B3 coatings, Fig. 5(a,c) respectively, and for 637.6 cm^{-1} monoclinic peak of B2 and B3 coatings, Fig. 5(b,d) respectively. These peak shifts can be quantified into stress using the piezo-spectroscopic coefficients and the Raman shift and piezo-spectroscopic relationship equation, Eq. (1).

It can be observed that after 1 h of annealing that, overall, the tetragonal peak has red shifted towards tension as well as the monoclinic peak. Then after 10 h of annealing, the tetragonal peak has shifted more to a blue shift in compression. The monoclinic peak for 10 h of annealing, while split, has more of a compressive blue shift, similar to the tetragonal peak at 10 h, but has also retained its tensile red shift in some areas. The red and blue shifts in the monoclinic peak corresponds to both microstructure as well as the presence and concentration of the monoclinic phase in those regions. Areas with a lower presence of the monoclinic phase will naturally have a weaker Raman signal than regions with higher monoclinic concentrations.

In addition to the 643.78 cm^{-1} tetragonal peak, the 463.7 cm^{-1} peak has also been used previously in literature to measure the stress of the non-transformable tetragonal phase [21,44]. The 463.7 cm^{-1} peak was used as a form of validation of the results within this study. For this validation the unstressed reference peak position is 463.7 cm^{-1} [21,44] and the piezo-spectroscopic coefficient used is 5.6 cm^{-1} GPa^{-1} [44]. It should be noted that this coefficient is for air plasma sprayed 5YSZ, meaning some minor discrepancy will be present as compared to what the coefficient would be for the 463.7 cm^{-1} peak for EB-PVD 7YSZ. Similarly, a 488 nm Ar/Kr laser was reported in Krämer et al. [21], compared to the 532 nm He/Ne laser used within this study. The stress for the 463.7 cm^{-1} peak is reported in Fig. 6. A similar trend in the localized stress distribution between the intercolumnar gaps and on and at the edge of the columns to what was found in Fig. 4 is observed. However, there are differences within the overall average stress states throughout the depth. Most notably, the overall reported stress state within the non-infiltrated sample (Fig. 6(a)), while uniform, is estimated at nearly 1 GPa in tension. While high, using the residual stress within the non-infiltrated sample as a reference for the infiltrated, it is observed that both the infiltrated samples are more in compression relative to the non-infiltrated sample. The localized microstructural effects on the stress distribution also influence the stress state of the probed volume. The intercolumnar gaps tend to be less compressive than on or at the edge of the columns.

5. Discussion

A schematic of the stress evolution of the coating as a result of CMAS infiltration summarizing our observations is shown in Fig. 7. Fig. 7(a) is a schematic of the pristine columnar microstructure prior to CMAS infiltration. The columnar tips are well defined and feather arms can be observed along the edges of these columnar finger-like

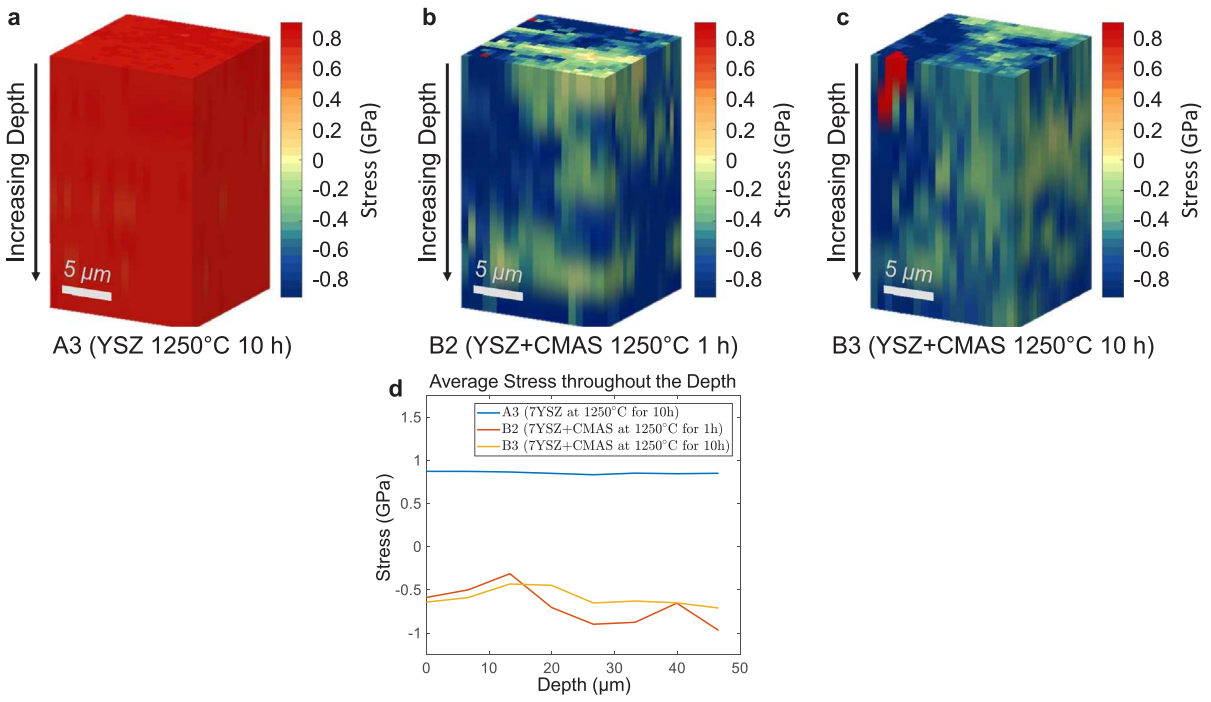

Fig. 6. 3D reconstruction of the stress for the 463.7 cm^{-1} peak. (a) a non-infiltrated 7YSZ sample annealed at 1250 °C for 10 h (A3), (b) a CMAS infiltrated 7YSZ sample annealed at 1250 °C for 1 h (B2), and (c) a CMAS infiltrated 7YSZ sample annealed at 1250 °C for 10 h (B3) as well as (d) the average stress as a function of depth for all three samples.

structures. The center of these columns would be in compression and a stress gradient to a less stressed or more neutral state is present approaching the edge of these columns. As molten CMAS deposits onto the surface of the coating, as seen in Fig. 7(b), it infiltrates to some depth as seen in Fig. 7(c). Distinct stress regions form, which can be distinguished between the infiltrated and non-infiltrated zones of the coating. These differences in the stress state of the coating within these two zones matches with literature [21]. The depth at which the CMAS infiltrates is dependent on the operating temperatures as well as infiltration time. With the thermal gradient present from the surface of the coating to the interface of the coating, bond coat, and substrate, commonly the CMAS will infiltrate to a certain depth and solidify as it reaches below melting temperatures within the coating. This infiltration can also be interrupted if the operating temperatures of the turbine decreases. Depending on the temperature, the CMAS might not solidify, resulting in full infiltration of the entire thickness of the coating. At the beginning of CMAS exposure, the effects of infiltration depth on the residual stress of the coating is immediately observable [52].

Primarily two different types of stresses are introduced during infiltration. The first is purely mechanical and the second is purely chemical. The mechanical stress comes as the coating sinters as well as stiffens when the CMAS solidifies within an infiltrated region and displays a tensile stress state similar to that observed during aging with the bulk splat-like microstructure of air plasma sprayed coatings [41,53]. In this case, the solidified CMAS would start to pull the columns of the coating in tension and cause a stress gradient from the edge of these columns to the column center. This stress is also fast acting, occurring immediately upon CMAS solidification and will be the predominant stress contributor early in the coating's exposure to CMAS. Depending on the extent and intensity of this additional residual stress, the coating may already start to fail through the formation, propagation, and coalescence of cracks [35]. The chemical stress occurs over longer periods of exposure and over several cycles of temperature fluctuations. Phase destabilization leading to phase transformation occurs upon cooling below approximately 600 °C within the yttria-lean parts of the 7YSZ. This leads to the transformation of the tetragonal phase to the monoclinic phase [32]. As observed in a previous investigation in this work [39], a majority of this phase transformation into the monoclinic phase occurs by 1 h of CMAS exposure and infiltration and only slightly increases by 10 h. Though it should also be noted that the concentration and extent of this phase transformation throughout the probed volume becomes more developed over time. The newly transformed monoclinic phase induces a compressive force onto the surrounding coating due to its volumetric expansion during phase transformation. Since this stress is dependent on the concentration and on the rate of monoclinic phase volume fraction growth, this stress is slow acting and becomes more dominant over longer exposure times. In high enough concentrations, this chemically-induced stress would negate the aforementioned mechanically-induced tensile stress and push the coating into a residual stress profile of compression.

Outside of this infiltrated region, the coating would behave as it did prior to CMAS deposition. However, as represented in Fig. 7(c), an interface between the infiltrated and non-infiltrated regions would result in some mismatch between the residual stress states. This intermixed stress region would introduce a gradient between the two stress states of the infiltrated and non-infiltrated and would depend on additional parameters, such as, but not limited to, the infiltration depth and the age of the coating. It is at this interface zone that cracks and CMAS-related spallation are be most likely to occur, especially when considering the accumulation of stresses at the interface [54], coefficient of thermal expansion mismatch, and thermal loading during an operational cycle.

The monoclinic phase volume fraction (mPVF), as previously described in [39], and its relationship to stress can be observed in Fig. 8. For Fig. 8(a,b), mPVF and stress stack maps throughout the depth of the coating are shown for both CMAS-infiltrated samples for 1 h of annealing, Fig. 8(a), and 10 h of annealing, Fig. 8(b). Within both of these stack maps are highlighted regions displaying relatively low and high mPVF concentrations for each sample. All mPVF and stress measurements within the low and high mPVF regions were then averaged throughout the depth and are summarized in Fig. 8(c,d). For the CMAS infiltrated sample annealed at 1250 °C for 1 h, Fig. 8(a,c), it can be observed that regions with low mPVF are more in tension as compared

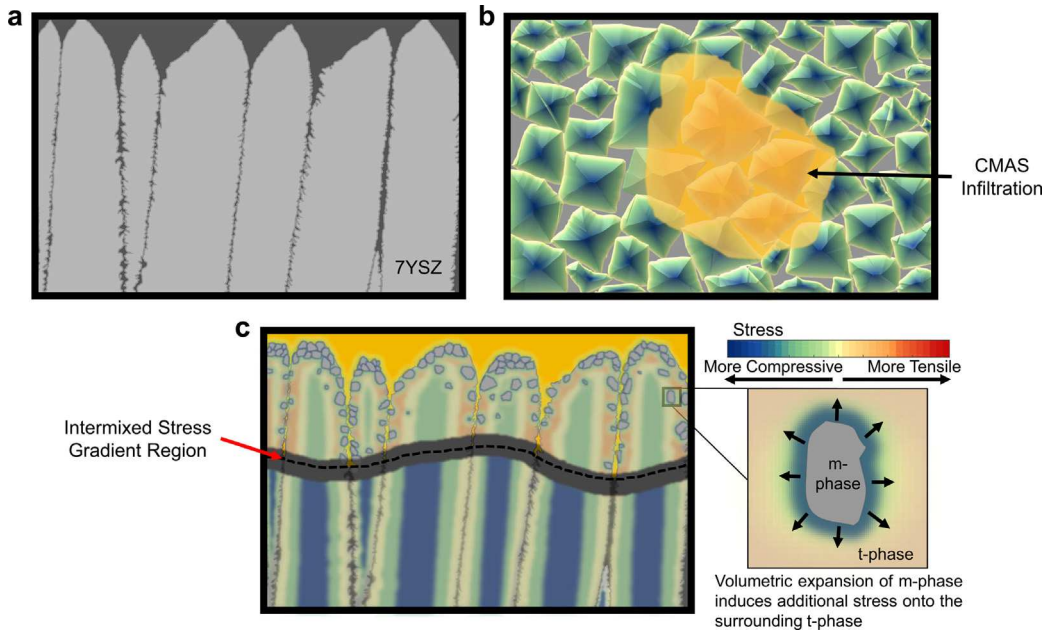

Fig. 7. Residual stress schematic of a CMAS infiltrated 7YSZ EB-PVD coating. Schematics of (a) a pristine 7YSZ EB-PVD coating cross-section prior to any CMAS exposure or infiltration. (b) Top-down view of the 7YSZ EB-PVD coating, showing cut aways of the columns as well as a region for CMAS infiltration. The typical stresses experienced by the coating is highlighted where compressive stresses are blue and slowly shift towards green until reaching a relatively unstressed state indicated in yellow. Stresses are scaled with high tensile stresses in red and are shifted to orange as the stresses approach a relatively unstressed state indicated in yellow. The stresses then slowly shift to green and finally blue as the stresses become more compressive. (c) The cross-section of the 7YSZ EB-PVD coating after some time that CMAS as infiltrated and interacted with the coating, allowing for substantial monoclinic formation to occur. Two distinct regions form: the CMAS infiltrated and the non-infiltrated regions. An intermixed stress region forms at the interface between these two regions. The overall stress gradient within this intermixed region is dependent on several factors including, but not limited to, CMAS infiltration depth, coating age and the TGO growth development. The localized stress gradient induced by the formation of the monoclinic phase (m-phase) is highlighted to the right of (c) where compressive forces, relative to the surrounding tetragonal phase of the coating, are present around the globular monoclinic phase. (For interpretation of the references to color in this figure legend, the reader is referred to the web version of this article.)

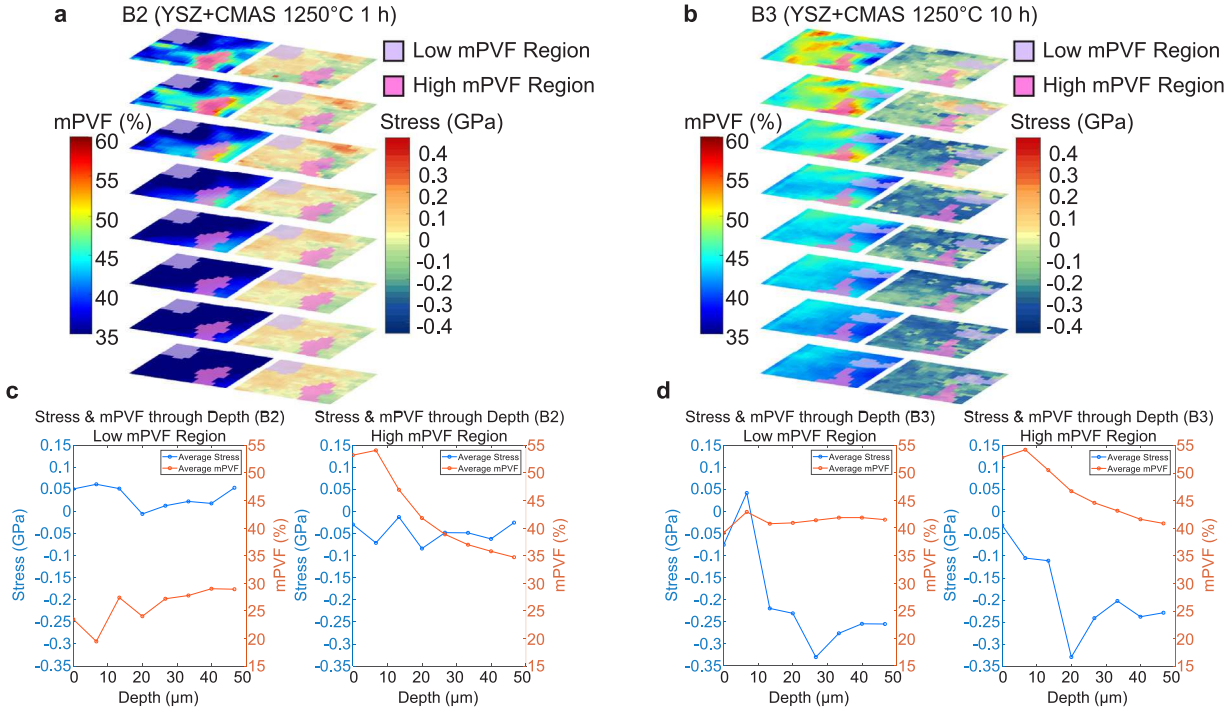

Fig. 8. Localized mPVF and residual stress comparison. A comparison of the localized monoclinic phase concentrations, measured through the phase volume fraction (mPVF) [39], and the localized stress state of the probed areas throughout the probed depth of the coating are shown for samples infiltrated by CMAS annealed at 1250 °C for (a) 1 h and (b) 10 h. For both samples, relatively low and high mPVF regions were selected and mPVF and stress were tracked within these regions throughout the depth of the coating for the (c) 1 h and (d) 10 h samples.

to region with high mPVF, which are more in compression. This can be observed in the average stress and mPVF throughout the depth plots for the low and high mPVF regions. On average, the stress in the low mPVF region is around 50 MPa in tension. The mPVF varies between 20%–30% in this low mPVF region. The stress being in tension follows what has been observed in literature for CMAS exposed coatings with little phase transformation [24,26]. Meanwhile, the stress in the high mPVF region is around 50 MPa in compression. The mPVF in this high region starts around 55% and decreases towards around 35% around 46 μm into the depth of the coating.

As the monoclinic phase becomes more developed throughout the probed volume of the coating after annealing a CMAS infiltrated sample at 1250 °C for 10 h, Fig. 8(b,d), the stress does not vary as drastically between low and high mPVF regions relative to the sample. Both regions have an average stress starting around 50 MPa in compression at the surface and becomes more compressive throughout the depth of the coating until reaching around 250 MPa in compression around 46 μm into the depth of the coating. The low mPVF region is relatively consistent throughout the depth of the coating with a mPVF at around 40%. The high mPVF region starts around 55% and decreases to around 40% around 46 μm into the depth of the coating.

Comparing the 1 h and 10 h annealing samples, it can be observed that there is some threshold range of mPVF, in which the residual stress state of the coating is dependent on. Below this threshold, the additional residual stresses introduced by CMAS infiltration are dominated primarily by physical mechanisms, such as coating stiffening. Above this threshold, the additional stresses introduced are dominated more by chemical mechanisms, such as the phase transformation of the coating. Finally, as the mPVF approaches this threshold, the stress state of the coating would slowly shift from tension to compression, as what is seen between the low and high mPVF regions for the 1 h annealed sample in Fig. 8(c). This trend has also been noted in literature [21,50]. It is noted that additional exposure studies with a more comprehensive annealing time sample matrix between 1 h and 10 h would be needed to better define this transitional point and to observe how this value may change due to varying coating conditions and aging. From the results in Fig. 8(c,d), the transition from tension to compression appears around a mPVF of 35% for EB-PVD 7YSZ coatings exposed to CMAS early in its lifetime. This is observed in the 1 h annealed sample where the residual stress shifts from being in tension for the low mPVF region to compression for the high mPVF region. This shift into compression is continued when comparing the high mPVF region of the 1 h annealed sample, Fig. 8(c) with the low mPVF region of the 10 h annealed sample, Fig. 8(d). An increase in the mPVF, when comparing the low mPVF region and the high mPVF region of the 10 h annealed sample, has minimal effects on the residual stresses of the coating beyond an mPVF of 40%.

A linear Karl Pearson Correlation Coefficient calculation, Eq. (2), was performed to establish a correlation relationship between the mPVF and stress at varying monoclinic concentrations, where R is the correlation coefficient, n is the sample size, mPVF is the concentration of mPVF at a given point, and σ is the stress calculated at a given point. The resulting correlation coefficients calculated can be seen in Table 2. Eq. (2) is the linear Karl Pearson Correlation Coefficient equation and this equation provides a linear coefficient value between −1 to 1, where −1 would indicate a purely negative linear relationship in which there is an inversely proportional relationship trend between the mPVF and stress. Conversely, 1 would indicate a purely positive linear relationship in which there is a proportional relationship trend between the mPVF and stress. Another important value would be 0, which would indicate no linear relationship between the mPVF and stress values.

$$R = \frac{n\Sigma(mPVF\sigma) - (\Sigma mPVF)(\Sigma\sigma)}{\sqrt{[n\Sigma(mPVF^2) - (\Sigma mPVF)^2][n\Sigma(\sigma^2) - (\Sigma\sigma)^2]}} \quad (2)$$

Due to the varying mechanisms influencing stress, such as the mPVF concentration as observed in Fig. 8, all probed points on the surface measurement were put into one of three different sections: a low mPVF, medium mPVF, and high mPVF region. The range for each of these regions were determined relatively for each CMAS infiltrated sample by equally distributing the three ranges between the minimum mPVF value and the maximum mPVF value previously calculated. Since there is an uneven distribution of the mPVF values across the samples, the sample size is not consistent among the different regions and has been taken into consideration in the standard error calculations, Eq. (3).

Table 2
Pearson correlation coefficients between the calculated mPVF and stress, categorized by low mPVF, medium mPVF, and high mPVF ranges relative to the CMAS infiltrated 7YSZ samples annealed at 1250 °C for (B2) 1 h and (B3) 10 h. The correlation coefficient varies between −1, indicating a negative relationship, and 1, indicating positive relationship, with a coefficient near 0 would mean no relationship between the two measurements. A weak correlation would have a coefficient around 0.10–0.30, a medium correlation would be around 0.30–0.50, and a strong correlation would be around 0.50–1.00.

Sample	Low mPVF (0–20.2)	Medium mPVF (20.2–40.4)	High mPVF (40.4–60.5)
B2 (7YSZ + CMAS, 1250 °C for 1 h)	0.62 ± 0.08	0.97 ± 0.01	−0.93 ± 0.04
Sample	Low mPVF (36.8–43.9)	Medium mPVF (43.9–50.9)	High mPVF (50.9–58.0)
B3 (7YSZ + CMAS, 1250 °C for 10 h)	−0.91 ± 0.05	−0.95 ± 0.03	−0.90 ± 0.06

$$SE_R = \sqrt{\frac{1 - R^2}{n - 2}} \quad (3)$$

Strong correlations can be observed for both CMAS infiltrated samples across the low, medium, and high mPVF sections. This is expected since previous literature has established phase transformations having the ability to influence the overall stress state of the coating [30,52]. The low mPVF section for B2 (1250 °C, 1 h) has the lowest correlation coefficient, relative to the other coefficients and mPVF sections. This is explained by the chemical mechanisms influencing stress being weakest within the low mPVF section while the physical mechanisms being more dominant with a mPVF lower than the transitional point around 35% mentioned previously when comparing the mPVF and stress evolution throughout the depth in Fig. 8. The correlation coefficient value then increases through the transition from the physically dominant to chemically dominant mechanisms for the residual stress as the monoclinic concentration increases and the residual stress becomes compressive within the medium mPVF and high mPVF sections. The high mPVF section for the 1 h sample as well as all of the mPVF sections for the 10 h sample have a negative coefficient due to the notation of tensile stresses being “postive” and compressive stresses being “negative” in stress calculations. The 10 h sample, B3, as a relatively uniform correlation coefficient with little deviation across the low, medium, and high mPVF sections. This suggests that the transition to chemically dominated mechanisms impacting the overall residual stress profile of the coating the most has already been completed.

6. Conclusion

The work presented shows the evolution and changing prominence of both the physical and chemical mechanisms that dominate the localized stress state and microstructure of EB-PVD coatings evaluated through non-destructive confocal Raman spectroscopy. More specifically, CMAS infiltration introduces both additional physical and chemical components to the residual stress state of 7YSZ coatings. It was found for CMAS exposure on coatings cycled for a short time that thermomechanical degradation and additional physical mechanisms, such as coating stiffening, are more influential towards the overall residual stress state of the coating early on in CMAS exposure, as observed in the first hour of CMAS infiltration, producing a red Raman shift and inducing tensile loading of up to around 100 MPa onto the tetragonal ZrO_2 Raman bands of the 7YSZ coating. Then as the CMAS has more

time interact and destabilize the coating, thermochemical degradation and its chemical mechanisms, such as monoclinic formation, becomes a more dominant phenomenon, having a greater impact on the overall residual stress state of the coating and inducing a blue Raman shift and compressive loading on the tetragonal ZrO_2 up to around 100 MPa. These results also suggest a transitional concentration threshold of around 35% phase volume fraction. Below this threshold, the coating experiences tensile loading and its residual stress is dominated primarily by physical mechanisms. Above this threshold, the coating experiences compressive loading and its residual stress is dominated more by chemical mechanisms instead. On a microstructural level, the edges and surfaces of the EB-PVD columns were observed to be more sensitive to the residual stress effects from CMAS infiltration than regions with lower exposure to CMAS, such as the columnar cores and centers.

Declaration of competing interest

The authors declare that they have no known competing financial interests or personal relationships that could have appeared to influence the work reported in this paper.

Acknowledgments

The authors would like to acknowledge Chance Barrett for his sharing of the dataset for further analysis. Funding: This material is based upon work supported by National Science Foundation grants DMR 1337758, OISE 1460045, OISE 1952523 and by the German Aerospace Center, DEU (DLR).

References

[1] A.G. Evans, D. Mumm, J. Hutchinson, G. Meier, F. Pettit, Mechanisms controlling the durability of thermal barrier coatings, Prog. Mater. Sci. 46 (5) (2001) 505–553.
[2] R.A. Miller, Thermal barrier coatings for aircraft engines: history and directions, J. Therm. Spray Technol. 6 (1) (1997) 35–42.
[3] K. Knipe, A. Manero II, S.F. Siddiqui, C. Meid, J. Wischek, J. Okasinski, J. Almer, A.M. Karlsson, M. Bartsch, S. Raghavan, Inside the engine environment–synchrotrons reveal secrets of high-temperature ceramic coatings, Am. Ceram. Soc. Bull. 94 (1) (2015) 22.
[4] B. Liu, Y. Liu, C. Zhu, H. Xiang, H. Chen, L. Sun, Y. Gao, Y. Zhou, Advances on strategies for searching for next generation thermal barrier coating materials, J. Mater. Sci. Technol. 35 (5) (2019) 833–851.
[5] L. Shi, Z. Sun, Y. Lu, The combined influences of film cooling and thermal barrier coatings on the cooling performances of a film and internal cooled vane, Coatings 10 (9) (2020) 861.
[6] N.P. Padture, M. Gell, E.H. Jordan, Thermal barrier coatings for gas-turbine engine applications, Science 296 (5566) (2002) 280–284.
[7] W.A. Nelson, R.M. Orenstein, TBC experience in land-based gas turbines, J. Therm. Spray Technol. 6 (2) (1997) 176–180.
[8] U. Schulz, S. Terry, C. Levi, Microstructure and texture of EB-PVD TBCs grown under different rotation modes, Mater. Sci. Eng. A 360 (1–2) (2003) 319–329.
[9] R. Naraparaju, M. Hüttermann, U. Schulz, P. Mechnich, Tailoring the EB-PVD columnar microstructure to mitigate the infiltration of CMAS in 7YSZ thermal barrier coatings, J. Eur. Ceram. Soc. 37 (1) (2017) 261–270.
[10] M.P. Borom, C.A. Johnson, L.A. Peluso, Role of environment deposits and operating surface temperature in spallation of air plasma sprayed thermal barrier coatings, Surf. Coat. Technol. 86 (1996) 116–126.
[11] J.L. Smialek, The chemistry of Saudi Arabian sand: a deposition problem on helicopter turbine airfoils, in: Gordon Conference on Corrosion, 1991, NAS 1.15: 105234.
[12] C.G. Levi, J.W. Hutchinson, M.-H. Vidal-Sétif, C.A. Johnson, Environmental degradation of thermal-barrier coatings by molten deposits, MRS Bull. 37 (10) (2012) 932–941.
[13] R. Naraparaju, U. Schulz, P. Mechnich, P. Döbber, F. Seidel, Degradation study of 7 wt.% yttria stabilised zirconia (7YSZ) thermal barrier coatings on aero-engine combustion chamber parts due to infiltration by different CaO–MgO–Al2O3–SiO2 variants, Surf. Coat. Technol. 260 (2014) 73–81.
[14] P. Mechnich, W. Braue, Solid-state CMAS corrosion of an EB-PVD YSZ coated turbine blade: Zr4+ partitioning and phase evolution, J. Am. Ceram. Soc. 98 (1) (2015) 296–302.
[15] R. Naraparaju, J.J.G. Chavez, P. Niemeyer, K.-U. Hess, W. Song, D.B. Dingwell, S. Lokachari, C. Ramana, U. Schulz, Estimation of CMAS infiltration depth in EB-PVD TBCs: A new constraint model supported with experimental approach, J. Eur. Ceram. Soc. 39 (9) (2019) 2936–2945.
[16] M.R. Kabir, A.K. Sirigiri, R. Naraparaju, U. Schulz, Flow kinetics of molten silicates through thermal barrier coating: A numerical study, Coatings 9 (5) (2019) 332.
[17] X. Montero, R. Naraparaju, M. Galetz, U. Schulz, Study of CMAS infiltration and evaporation behaviour under water vapour/sulphur oxide conditions in EB-PVD 7YSZ, Corros. Sci. 198 (2022) 110123.
[18] C. Mercer, S. Faulhaber, A. Evans, R. Darolia, A delamination mechanism for thermal barrier coatings subject to calcium–magnesium–alumino-silicate (CMAS) infiltration, Acta Mater. 53 (4) (2005) 1029–1039.
[19] T.R. Kakuda, C.G. Levi, T.D. Bennett, The thermal behavior of CMAS-infiltrated thermal barrier coatings, Surf. Coat. Technol. 272 (2015) 350–356.
[20] J. Wu, H.-b. Guo, Y.-z. Gao, S.-k. Gong, Microstructure and thermo-physical properties of yttria stabilized zirconia coatings with CMAS deposits, J. Eur. Ceram. Soc. 31 (10) (2011) 1881–1888.
[21] S. Krämer, S. Faulhaber, M. Chambers, D.R. Clarke, C.G. Levi, J.W. Hutchinson, A. Evans, Mechanisms of cracking and delamination within thick thermal barrier systems in aero-engines subject to calcium-magnesium-alumino-silicate (CMAS) penetration, Mater. Sci. Eng. A 490 (1–2) (2008) 26–35.
[22] J.J.G. Chavez, R. Naraparaju, C. Mikulla, P. Mechnich, K. Kelm, C. Ramana, U. Schulz, Comparative study of EB-PVD gadolinium-zirconate and yttria-rich zirconia coatings performance against fe-containing calcium-magnesium-aluminosilicate (CMAS) infiltration, Corros. Sci. 190 (2021) 109660.
[23] H. Chang, C. Cai, Y. Wang, Y. Zhou, L. Yang, G. Zhou, Calcium-rich CMAS corrosion induced microstructure development of thermal barrier coatings, Surf. Coat. Technol. 324 (2017) 577–584.
[24] H. Peng, L. Wang, L. Guo, W. Miao, H. Guo, S. Gong, Degradation of EB-PVD thermal barrier coatings caused by CMAS deposits, Prog. Nat. Sci. Mater. Int 22 (5) (2012) 461–467.
[25] G. Pujol, F. Ansart, J.-P. Bonino, A. Malié, S. Hamadi, Step-by-step investigation of degradation mechanisms induced by CMAS attack on YSZ materials for TBC applications, Surf. Coat. Technol. 237 (2013) 71–78.
[26] S. Krämer, J. Yang, C.G. Levi, C.A. Johnson, Thermochemical interaction of thermal barrier coatings with molten CaO–MgO–Al2O3–SiO2 (CMAS) deposits, J. Am. Ceram. Soc. 89 (10) (2006) 3167–3175.
[27] M.A. Rivera-Gil, J.J. Gomez-Chavez, C. Ramana, R. Naraparaju, U. Schulz, J. Muñoz-Saldaña, High temperature interaction of volcanic ashes with 7YSZ TBC's produced by APS: Infiltration behavior and phase stability, Surf. Coat. Technol. 378 (2019) 124915.
[28] J.J.G. Chavez, R. Naraparaju, P. Mechnich, K. Kelm, U. Schulz, C. Ramana, Effects of yttria content on the CMAS infiltration resistance of yttria stabilized thermal barrier coatings system, J. Mater. Sci. Technol. 43 (2020) 74–83.
[29] R. Wellman, G. Whitman, J. Nicholls, CMAS corrosion of EB PVD TBCs: Identifying the minimum level to initiate damage, Int. J. Refract. Hard Met. 28 (1) (2010) 124–132.
[30] U. Schulz, Phase transformation in EB-PVD yttria partially stabilized zirconia thermal barrier coatings during annealing, J. Am. Ceram. Soc. 83 (4) (2000) 904–910.
[31] C. Viazzi, J.-P. Bonino, F. Ansart, Synthesis by sol-gel route and characterization of Yttria stabilized Zirconia coatings for thermal barrier applications, Surf. Coat. Technol. 201 (7) (2006) 3889–3893.
[32] H.F. Garces, B.S. Senturk, N.P. Padture, In situ Raman spectroscopy studies of high-temperature degradation of thermal barrier coatings by molten silicate deposits, Scr. Mater. 76 (2014) 29–32.
[33] D.M. Lipkin, J.A. Krogstad, Y. Gao, C.A. Johnson, W.A. Nelson, C.G. Levi, Phase evolution upon aging of air-plasma sprayed t-Zirconia coatings: I—Synchrotron X-Ray diffraction, J. Am. Ceram. Soc. 96 (1) (2013) 290–298.
[34] M. Ishigame, T. Sakurai, Temperature dependence of the Raman spectra of ZrO2, J. Am. Ceram. Soc. 60 (7–8) (1977) 367–369.
[35] L. Li, N. Hitchman, J. Knapp, Failure of thermal barrier coatings subjected to CMAS attack, J. Therm. Spray Technol. 19 (1) (2010) 148–155.
[36] R. Naraparaju, U. Schulz, S. Raghavan, E. Bohorquez, Non-destructive CMAS-infiltration characterization of thermal barrier coatings, 2020, Google Patents, US Patent 10, 837, 918.
[37] R. Naraparaju, U. Schulz, S. Raghavan, E. Bohorquez, Zerstörungsfreie cmas-infiltrationscharakterisierung von wärmesperrbeschichtungen, 2019.
[38] A.R. Krause, H.F. Garces, G. Dwivedi, A.L. Ortiz, S. Sampath, N.P. Padture, Calcia-magnesia-alumino-silicate (CMAS)-induced degradation and failure of air plasma sprayed yttria-stabilized zirconia thermal barrier coatings, Acta Mater. 105 (2016) 355–366.
[39] C. Barrett, Z. Stein, J. Hernandez, R. Naraparaju, U. Schulz, L. Tetard, S. Raghavan, Detrimental effects of sand ingression in jet engine ceramic coatings captured with Raman-based 3D rendering, J. Eur. Ceram. Soc. 41 (2) (2021) 1664–1671.
[40] V. Teixeira, M. Andritschky, W. Fischer, H. Buchkremer, D. Stöver, Analysis of residual stresses in thermal barrier coatings, J. Mater Process. Technol. 92 (1999) 209–216.

[41] A.M. Limarga, R. Vaßen, D.R. Clarke, Stress distributions in plasma-sprayed thermal barrier coatings under thermal cycling in a temperature gradient, J. Appl. Mech. 78 (1) (2011).
[42] M. Tanaka, R. Kitazawa, T. Tomimatsu, Y. Liu, Y. Kagawa, Residual stress measurement of an EB-PVD Y2o3-ZrO2 thermal barrier coating by micro-Raman spectroscopy, Surf. Coat. Technol. 204 (5) (2009) 657–660.
[43] P. Barberis, T. Merle-Méjean, P. Quintard, On Raman spectroscopy of zirconium oxide films, J. Nucl. Mater. 246 (2–3) (1997) 232–243.
[44] P. Bouvier, G. Lucazeau, Raman spectra and vibrational analysis of nanometric tetragonal zirconia under high pressure, J. Phys. Chem. Solids 61 (4) (2000) 569–578.
[45] P. Arunkumar, U. Aarthi, M. Sribalaji, B. Mukherjee, A.K. Keshri, W.H. Tanveer, S.-W. Cha, K.S. Babu, Deposition rate dependent phase/mechanical property evolution in zirconia and ceria-zirconia thin film by EB-PVD technique, J. Alloys Compd. 765 (2018) 418–427.
[46] V. Kypraiou, S. Pelekanos, G. Eliades, Identification of monoclinic phase in CAD/CAM zirconia FPD frameworks, Eur. J. Esthet. Dent. 7 (4) (2012) 418–429.
[47] B.-K. Kim, H.-o. Hamaguchi, Mode assignments of the Raman spectrum of monoclinic zirconia by isotopic exchange technique, Phys. Status Solidi b 203 (2) (1997) 557–563.
[48] Y. Sohn, K. Vaidyanathan, M. Ronski, E. Jordan, M. Gell, Thermal cycling of EB-PVD/MCrAlY thermal barrier coatings: II. evolution of photo-stimulated luminescence, Surf. Coat. Technol. 146 (2001) 102–109.
[49] M. Vidal-Setif, N. Chellah, C. Rio, C. Sanchez, O. Lavigne, Calcium–magnesium–alumino-silicate (CMAS) degradation of EB-PVD thermal barrier coatings: Characterization of CMAS damage on ex-service high pressure blade TBCs, Surf. Coat. Technol. 208 (2012) 39–45.
[50] G. Pezzotti, K. Yamada, S. Sakakura, R.P. Pitto, Raman spectroscopic analysis of advanced ceramic composite for hip prosthesis, J. Am. Ceram. Soc. 91 (4) (2008) 1199–1206.
[51] P. Yáñez-Contreras, M. León-Rodríguez, J.M. Medina-Flores, J.A. Jiménez-García, F.J. Santander-Bastida, J. Yáñez-Rodríguez, Determination of residual stresses in thermal barrier coating due to the amount of CMAS infiltration, Dyna 87 (215) (2020) 76–83.
[52] C. Chiu, S. Tseng, C. Chao, X. Fan, W. Cheng, Interfacial stresses of thermal barrier coating with film cooling holes induced by CMAS infiltration, Coatings 12 (3) (2022) 326.
[53] H. Dong, G.-J. Yang, C.-X. Li, X.-T. Luo, C.-J. Li, Effect of TGO thickness on thermal cyclic lifetime and failure mode of plasma-sprayed TBC s, J. Am. Ceram. Soc. 97 (4) (2014) 1226–1232.
[54] G. Xu, L. Yang, Y. Zhou, A coupled theory for deformation and phase transformation due to CMAS infiltration and corrosion of thermal barrier coatings, Corros. Sci. 190 (2021) 109690.